Research Article Vol. 10, No. 10 / 1 October 2019 / *Biomedical Optics Express* 5207

Biomedical Optics EXPRESS

Constrained polarization evolution simplifies depth-resolved retardation measurements with polarization-sensitive optical coherence tomography

QIAOZHOU XIONG,[1,6] NANSHUO WANG,[1,6] XINYU LIU,[1,3,6] SI CHEN,[1] CILWYN S. BRAGANZA,[1] BRETT E. BOUMA,[4,5] LINBO LIU,[1,2,7,8] AND MARTIN VILLIGER[4,7,9]

[1] *School of Electrical and Electronic Engineering, Nanyang Technological University, Singapore, 639798, Singapore*
[2] *School of Chemical and Biomedical Engineering, Nanyang Technological University, Singapore, 637459, Singapore*
[3] *Singapore Eye Research Institute, Singapore, 169856, Singapore*
[4] *Harvard Medical School and Massachusetts General Hospital, Wellman Center for Photomedicine, Boston, Massachusetts 02114, USA*
[5] *Institute for Medical Engineering and Science, Massachusetts Institute of Technology, Cambridge, Massachusetts 02139, USA*
[6] *These authors contributed equally*
[7] *These authors contributed equally*
[8] *Corresponding author: LIULINBO@ntu.edu.sg*
[9] *Corresponding author: MVILLIGER@mgh.harvard.edu*

Abstract: We observed that the polarization state of light after round-trip propagation through a birefringent medium frequently aligns with the employed input polarization state 'mirrored' by the horizontal plane of the Poincaré sphere. We explored the predisposition for this mirror state and evidence that it constrains the evolution of polarization states as a function of the round-trip depth into weakly scattering birefringent samples, as measured with polarization-sensitive optical coherence tomography (PS-OCT). Combined with spectral variations in the polarization state transmitted through system components, we demonstrate how this constraint enables measurement of depth-resolved birefringence using only a single input polarization state, which offers a critical simplification compared to conventional PS-OCT employing two input states.

1. Introduction

Polarization offers access to unique, distinguishing signatures of samples for diverse applications from remote sensing [1,2] to biomedical optics [3–5]. Polarization sensitive optical coherence tomography (PS-OCT) performs polarimetric measurements in combination with coherence gating and effectively measures the polarization state of light as a function of its round-trip path length into the sample [6–8]. Many fibrous tissues with important physiologic function, such as collagen, muscle, or nerve fibers, exhibit birefringence and cause a differential delay, or retardation, between light polarized parallel and orthogonal to the fibrillar tissue components. Observing the depth-dependence of the polarization state backscattered from a sample illuminated with a single input state provides the cumulative round-trip retardation from the tissue surface to a given depth in the tissue [9,10]. Because the rate of polarization change depends on the alignment of the polarization state with the local optic axis in the sample, it is in general very difficult to interpret cumulative retardation. Furthermore, whenever the polarization state aligns with the optic axis in the sample, it ceases to evolve and may mask birefringent tissue areas. Conventionally,

#372371
Journal © 2019
https://doi.org/10.1364/BOE.10.005207
Received 15 Jul 2019; revised 28 Aug 2019; accepted 31 Aug 2019; published 17 Sep 2019

multiple input polarization states are employed [11] in addition to polarization-diverse detection to fully characterize the polarization properties of a sample and compute local retardation, i.e. depth-resolved tissue birefringence [12–16]. Alleviating the demanding hardware requirements for local retardation imaging would enable more widespread exploration of this compelling contrast mechanism.

In previous experiments, we observed that the polarization state of backscattered or reflected light, when measured through identical illumination and detection paths, frequently evolved through the employed input polarization state but with reversed handedness, corresponding to the input state mirrored by the horizontal plane of the Poincaré sphere [17]. Earlier investigations of the polarization properties of single mode fibers reported on aspects of the polarization mirror state [18–20], yet without elucidating its manifestation. Here, we experimentally and theoretically evidence the propensity for this mirror state and show how it constrains the evolution of the depth-dependent polarization state. We then employ this constraint to perform local retardation imaging of optical phantoms and *ex vivo* tissue using a single input polarization state, both with free-space and catheter-based PS-OCT implementations. Taking into account minor spectral variations in the polarization state transmitted through system components we obtain local retardation maps that avoid the accidental masking of tissue birefringence.

2. Experimental methods

2.1. Polarization sensitive optical coherence tomography

A single input state polarization-sensitive spectral domain optical coherence tomography (PS-SD-OCT) system was configured as shown in Fig. 1. The unpolarized light from a super-continuum source (DK-3460, NKT Photonics Inc.) was polarized by cascading a horizontal linear polarizer (P1, LPNIRE100-B, Thorlabs Inc.) with an achromatic quarter-wave plate oriented at 45° (Q1, AQWP10M-980, Thorlabs Inc.) to obtain circular polarization, unless otherwise noted, and then split by a free-space beamsplitter (50:50, BS014, Thorlabs Inc.) into the reference and sample arms. A linear polarizer (P2, LPNIRE100-B, Thorlabs Inc.) oriented at 45° in the reference arm ensured identical reference spectra for both channels of the polarization-diverse detection. In each of the interferometer arms, by means of a flip-mirror, the light was directed either in free space to the sample and the reference mirror, respectively, or first coupled through 1.5 m of single mode fiber. A three-paddle polarization controller was applied in each fiber for polarization management. For sample imaging, the light in the sample arm was focused with a 30 mm focal length lens, achieving a full width at half maximum (FWHM) spot diameter of 8 µm, and scanned with galvanometric mirrors in both lateral directions. At the exit port of the beamsplitter, a half-wave plate (H1, AHWP10M-980, Thorlabs Inc.) allowed precise alignment of the polarization axes of the sample and reference light with the slow and fast axis of a piece of polarization-maintaining (PM) fiber (P3-780PM-FC-2, Thorlabs Inc.). The polarization states of the PM fiber were subsequently split with a polarizing beamsplitter towards two identical, custom-built spectrometers, described in detail previously [21], to record the interference pattern of the horizontal (X) and vertical (Y) polarization components, respectively. The detected source bandwidth was about 160 nm centered at 840 nm, providing a measured axial resolution of 2.5 µm in air. Recorded spectra were pre-processed by background-subtraction, alignment between the two spectrometers [22], interpolation to linear wavenumber k, and compensation for dispersion imbalance between the sample and reference arms [21].

Catheter-based imaging of birefringent phantoms was performed with a polarization-sensitive optical frequency domain imaging (PS-OFDI) system, as described previously [23]. In short, the system operated at a center wavelength of 1300 nm, scanning a range of 110 nm. The system employed polarization-diverse detection and an illumination modulation scheme, whereby the source polarization state was alternated for subsequent A-lines between two states located

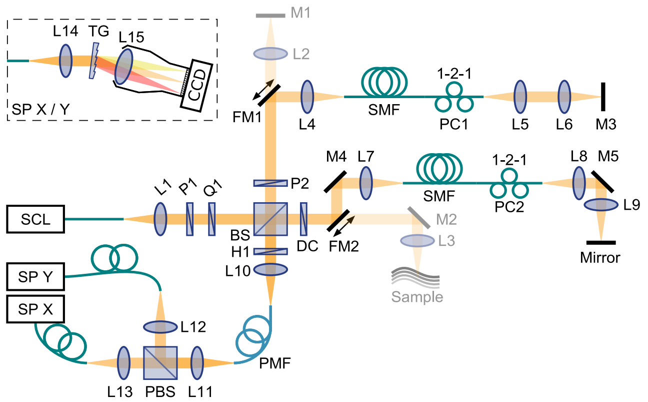

Fig. 1. A detailed schematic of the imaging system. SCL: super-continuum laser, L1-15: achromatic lenses (Thorlabs Inc.), P1-2: polarizers, Q1: quarter-wave plate, H1: half-wave plate, BS: non-polarizing beamsplitter, PBS: polarizing beamsplitter, DC: dispersion compensator (BK7 glass plate), M1-5: mirrors, FM1-2: flip mirrors. SP: spectrometer. TG: transmission grating, SMF: single-mode fiber, PMF: polarization-maintaining fiber, PC1-2: polarization controllers, both with 1, 2 and 1 fiber coils in the three paddles, respectively.

orthogonal to each other on the Poincaré sphere. The imaging console interfaced with commercial intravascular catheters (FastView, Terumo).

2.2. Sample preparation

To fabricate birefringence phantoms, we cut bands from scattering films of acrylonitrile butadiene styrene (ABS) and stretched them after heating them above their glass-transition temperature, similar to our previous work [23]. The first phantom assembled a stack of three birefringent bands oriented at around 30° and 60° with respect to the first layer. The second phantom comprised one long band above four parallel shorter segments with distinct birefringence, oriented at 45°. The bands of both phantoms were embedded in ultrasound gel mixed with polystyrene beads (Polysciences Inc., 300 nm in diameter) with a concentration of $\sim 5 \times 10^{10}/\mathrm{mL}$ to provide a non-birefringent scattering matrix.

Retinal imaging was performed on swine eyes, collected from a local slaughterhouse. The imaging was carried out within two hours after the eyeball was harvested. We cut the eyeball along the equator, removed the lens, emptied the vitreous chamber, and instilled just enough saline to prevent specular reflection while scanning the retina.

3. Polarization constraint in reciprocal unitary backscattering

3.1. Experimental manifestation

3.1.1. Round-trip transmission through fiber

To examine the polarization mirror state, we first measured the round-trip signal through a 1.5 m long single-mode optical fiber, reflected off an attenuated mirror. Employing a polarization controller to dynamically alter the birefringence of the fiber, we measured the time-varying polarization state at the central wavenumber resulting from randomly moving the paddle positions of the controller. Visualized as a normalized Stokes vector in the Q, U, and V-coordinates of the Poincaré sphere in Fig. 2, the polarization state distinctly evolves multiple times through a specific state $\mathbf{m}$. Repeated with different launching polarization states $\mathbf{s}$, which were measured by reflecting the light to the detector before entering the fiber, we identified the state $\mathbf{m} = \mathbf{D} \cdot \mathbf{s}$, where $\mathbf{D} = \mathrm{diag}(1, 1, -1)$, as the input state mirrored by the horizontal QU-plane, and designated it as the polarization mirror state. The sequence of the three paddles in the polarization controller is designed to be able to reach any possible output state after forward transmission, and the measured polarization states indeed cover the majority of the Poincaré sphere, yet there is an obvious predisposition for the polarization states to evolve through the mirror state. Of note, all measurements were performed in the fixed coordinates of the receiver and are independent of the orientation of the coordinates in the illumination path [24,25].

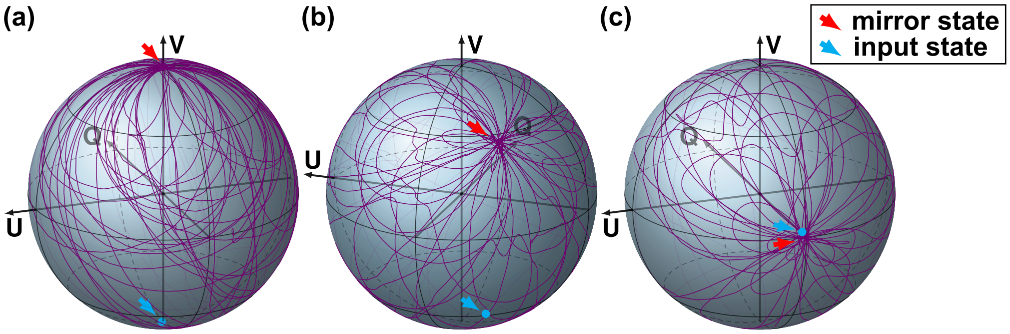

Fig. 2. Demonstration of the polarization mirror state. (a)–(c) Polarization state evolution on the Poincaré sphere as a result of moving the three paddles of the PC when using circularly, elliptically and linearly polarized input states, respectively, indicated by the blue arrows, resulting in the repeated crossing of the mirror state, indicated by the red arrows.

3.1.2. Depth-resolved polarization states

Next, we investigated the depth-resolved polarization states in a birefringence phantom consisting of three linearly birefringent layers with distinct optic axis orientations. Without the fiber segment in the interferometer arms, the phantom was imaged with the free space configuration of the system. At each scanning location, using PS-OCT, we constructed the Stokes vector as a function of depth in the sample. To remove speckle and improve the signal, we spatially filtered the original Stokes vectors with a two-dimensional Gaussian kernel of 20 µm $1/e^2$ width in the axial direction and 80 µm in the lateral direction. Finally, we computed the normalized three-component Stokes vector $\mathbf{t}(z)$ as a function of depth, shown in Fig. 3(b-d) for three distinct input polarization states (indicated by blue arrows) at one lateral location. Inspection of the traces reveals that within each of the linearly birefringent layers the polarization state evolves on a circle which passes through the mirror state $\mathbf{m}$ (indicated by red arrows). Fitting circles that approximate the data and pass through $\mathbf{m}$ (in purple color) indeed demonstrate a close match with the measured polarization states. Each layer defines a distinct circle intersecting with the circle of the next layer at the polarization state reflected from the interface between the layers. The realization of the mirror state and the polarization traces is entirely dependent on the specific input state.

3.2. Theoretical derivation

To appreciate the mirror state phenomenon, we express the depth-dependent polarization state $\mathbf{t}(z)$ as a function of the input state $\mathbf{s}$, transformed under the effect of the round trip through the sample $\mathbf{T}(z)$:

$$\mathbf{t}(z) = \mathbf{T}(z) \cdot \mathbf{s}. \tag{1}$$

Considering the single-pass forward transmission $\mathbf{N}(z)$, we can express the round trip as:

$$\mathbf{T}(z) = \mathbf{D} \cdot \mathbf{N}^{\top}(z) \cdot \mathbf{D} \cdot \mathbf{N}(z). \tag{2}$$

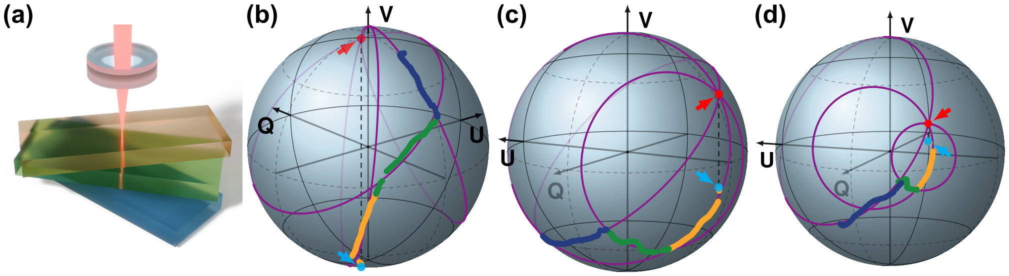

Fig. 3. Evolution of coherence-gated polarization states in a three-layer birefringence phantom. (a) Schematic sketch of the phantom consisting of three layers with distinct optic axis orientations. (b)–(d) Polarization state evolution (color-coded corresponding to the layers in (a)) for a circularly polarized (b), elliptically polarized (c), and linearly polarized input state (d). Input polarization states are indicated by the blue arrows. Red arrows point to the mirror states.

In reciprocal media, the reverse transmission through element $\mathbf{N}$ is described by $\mathbf{D}\cdot\mathbf{N}^\top\cdot\mathbf{D}$ [26–28] (Appendix 7.1). We assume the sample transmission to be purely retarding and ignore the effects of depolarization and diattenuation, which allows expressing the polarization states as normalized three-component vectors. The retardation matrices belong to the special orthogonal group SO(3) and define a rotation of the polarization states in the Poincaré sphere around a rotation axis, or optic axis. The round trip matrix $\mathbf{T} = \mathbf{D}\cdot\mathbf{T}^\top\cdot\mathbf{D}$ is by construction D-transpose symmetric, which cancels any circular retardation of $\mathbf{N}$ (V-component of the rotation axis) and confines the rotation axis of $\mathbf{T}$ to the QU-plane, enforcing it to be a linear retarder.

For the input state $\mathbf{s}$ to be mapped to its mirror state $\mathbf{m} = \mathbf{T}\cdot\mathbf{s} = \mathbf{D}\cdot\mathbf{s}$, it has to be invariant under transformation by $\mathbf{D}\cdot\mathbf{T}$, i.e. it has to be an eigenvector of $\mathbf{D}\cdot\mathbf{T}$ associated with a unitary eigenvalue ($\mathbf{T}$ can never be $\mathbf{D}$ because $\det(\mathbf{T}) = 1$ and $\det(\mathbf{D}) = -1$). As we show in the Appendix by geometric construction (Appendix 7.2), for each possible orientation of the optic axis of $\mathbf{T}$ within the QU-plane, there exists a defined amount of retardance to fulfill this condition. Each time the polarization state evolves through the mirror state in Fig. 2, the round-trip retardation matrix through the polarization controller generated a suitable combination of optic axis orientation and retardation to map the input state onto the mirror state. To map the input state onto any other state, there exists only a unique optic axis orientation and retardation, which offers an intuitive explanation for the propensity of the mirror state.

To further investigate the depth-resolved polarization state $\mathbf{t}(z)$ and its evolution through the mirror state, we take its derivative with respect to depth:

$$\frac{\partial \mathbf{t}(z)}{\partial z} = \frac{\partial \mathbf{T}(z)}{\partial z}\cdot\mathbf{s} = \frac{\partial \mathbf{T}(z)}{\partial z}\cdot\mathbf{T}^\top(z)\cdot\mathbf{t} = \boldsymbol{\beta}\times(z)\cdot\mathbf{t}. \tag{3}$$

In analogy with the differential Mueller matrix formalism $\boldsymbol{\beta}\times$ is the differential retardation operator. Because $\mathbf{T}\cdot\mathbf{T}^\top$ is the identity matrix enforcing $(\partial\mathbf{T}/\partial z)\cdot\mathbf{T}^\top = -\mathbf{T}\cdot\left(\partial\mathbf{T}^\top/\partial z\right)$, $\boldsymbol{\beta}\times$ is skew-symmetric and corresponds to taking the cross-product with vector $\boldsymbol{\beta} = \left[\beta_\mathrm{Q}, \beta_\mathrm{U}, \beta_\mathrm{V}\right]$:

$$\boldsymbol{\beta}\times = \begin{bmatrix} 0 & -\beta_\mathrm{V} & \beta_\mathrm{U} \\ \beta_\mathrm{V} & 0 & -\beta_\mathrm{Q} \\ -\beta_\mathrm{U} & \beta_\mathrm{Q} & 0 \end{bmatrix} = \gamma\cdot\hat{\boldsymbol{\beta}}\times. \tag{4}$$

$\hat{\boldsymbol{\beta}}$ is the normalized optic axis and γ, the norm of vector $\boldsymbol{\beta}$, is the local retardation, i.e. the rate at which the retardation increases with depth. Specifically, $\gamma = 2k\Delta n$, with k the wavenumber and

Δn the birefringence. Using Eq. (2) to express $\boldsymbol{\beta}\times$ provides

$$\boldsymbol{\beta}\times = \mathbf{D}\cdot\mathbf{N}^\top\cdot\mathbf{D}\cdot\underbrace{\left(\mathbf{D}\cdot\mathbf{N}\cdot\frac{\partial\mathbf{N}^\top}{\partial z}\cdot\mathbf{D}+\frac{\partial\mathbf{N}}{\partial z}\cdot\mathbf{N}^\top\right)}_{\boldsymbol{\tau}\times}\cdot\mathbf{D}\cdot\mathbf{N}\cdot\mathbf{D} = \mathbf{D}\cdot\mathbf{N}^\top\cdot\mathbf{D}\cdot\boldsymbol{\tau}\times\cdot\mathbf{D}\cdot\mathbf{N}\cdot\mathbf{D}. \quad (5)$$

$\boldsymbol{\tau}\times$ is not only skew-symmetric, but also D-transpose symmetric, confining $\hat{\boldsymbol{\tau}}$ to the QU-plane. However, the similarity transformation of $\boldsymbol{\tau}\times$ by $\mathbf{D}\cdot\mathbf{N}^\top\cdot\mathbf{D}$ rotates the apparent optic axis $\hat{\boldsymbol{\beta}}$ out of the QU-plane, in general. Re-integrating $\partial\mathbf{t}/\partial z$ at a given depth we obtain the first-order approximation to the evolution of $\mathbf{t}$:

$$\mathbf{t}'(z+\Delta z) = \exp\left(\Delta z\cdot\boldsymbol{\beta}\times\right)\cdot\mathbf{t}(z) = \mathbf{D}\cdot\mathbf{N}^\top\cdot\mathbf{D}\cdot\exp\left(\Delta z\cdot\boldsymbol{\tau}\times\right)\cdot\mathbf{N}\cdot\mathbf{s}. \quad (6)$$

where we used $\mathbf{t} = \mathbf{D}\cdot\mathbf{N}^\top\cdot\mathbf{D}\cdot\mathbf{N}\cdot\mathbf{s}$ and the property of the matrix exponential $\exp\left(\mathbf{A}\cdot\mathbf{B}\cdot\mathbf{A}^{-1}\right) = \mathbf{A}\cdot\exp(\mathbf{B})\cdot\mathbf{A}^{-1}$. Here, Δz determines the amount of retardance of the linear retarder $\exp\left(\Delta z\cdot\boldsymbol{\tau}\times\right)$, and as previously observed, it is always possible to find the suitable Δz, modulo $2\pi/\gamma$, for the given orientation of $\hat{\boldsymbol{\tau}}$ within the QU-plane to make $\mathbf{N}\cdot\mathbf{s}$ invariant to the transformation by $\mathbf{D}\cdot\exp\left(\Delta z\cdot\boldsymbol{\tau}\times\right)$ leading to $\mathbf{t}' = \mathbf{D}\cdot\mathbf{N}^\top\cdot\mathbf{N}\cdot\mathbf{s} = \mathbf{m}$. Hence, the first order approximation of the polarization state evolution at a given depth lies on a circle evolving (periodically) through the mirror state. Because $\boldsymbol{\tau}\times$ is constant within a homogeneously birefringent sample layer the first order evolution is independent of depth within this layer, and the polarization state follows closely the approximated circle. For the experiment of dynamically changing the fiber transmission, the derivative with respect to time instead of depth leads to the same conclusion that the first order approximation of the polarization state evolution at a given point of time lies on a circle evolving through the mirror state.

The mirror state constraint still manifests even when the overall system is not D-transpose symmetric. In a general case, static single-pass components $\mathbf{P}$ and $\mathbf{Q}$ alter the polarization states before and after the D-transpose symmetric transmission $\mathbf{T}(z)$ to yield to observed polarization state $\mathbf{t}(z) = \mathbf{Q}\cdot\mathbf{T}(z)\cdot\mathbf{P}\cdot\mathbf{s}$. While $\mathbf{T}(z)$ is intrinsically D-transpose symmetric and hence a linear retarder, the presence of $\mathbf{Q}$ and $\mathbf{P}$ modifies the overall transmission to become a general retarder [28]. However, $\mathbf{P}\cdot\mathbf{s}$ merely defines a modified input state $\mathbf{s}' = \mathbf{P}\cdot\mathbf{s}$, which upon transmission through $\mathbf{T}(z)$ repeatedly evolves through the mirror state $\mathbf{D}\cdot\mathbf{s}'$. The unitary matrix $\mathbf{Q}$ simply rotates this polarization state evolution and maps the apparent mirror state to the observed mirror state $\mathbf{m} = \mathbf{Q}\cdot\mathbf{D}\cdot\mathbf{P}\cdot\mathbf{s}$. In other words, with the presence of static, and possibly distinct, system components, the 'input' polarization state observed at the receiver in the absence of any sample transmission is $\mathbf{Q}\cdot\mathbf{P}\cdot\mathbf{s}$. The mirror state phenomenon ensures that the evolution of the polarization state including propagation through the sample $\mathbf{T}(z)$ evolves through the mirror state $\mathbf{Q}\cdot\mathbf{D}\cdot\mathbf{P}\cdot\mathbf{s} = \mathbf{Q}\cdot\mathbf{D}\cdot\mathbf{Q}^\top\cdot(\mathbf{Q}\cdot\mathbf{P}\cdot\mathbf{s})$. Here $\mathbf{Q}\cdot\mathbf{D}\cdot\mathbf{Q}^\top$ defines a new symmetry plane, which is moved from the QU-plane defined by $\mathbf{D}$ under the similarity transformation by $\mathbf{Q}$.

4. Local retardation imaging

4.1. Reconstruction of local retardation with single input state PS-OCT

Using a single circular input polarization state for PS-OCT, it is straightforward to compute the cumulative retardation that propagation through the sample to a given depth and back imparts on the input polarization state [6,10]. Yet, cumulative retardation can be difficult to interpret in samples with a layered architecture, and it is more insightful to compute the local retardation γ which is proportional to the sample birefringence at that depth location [12–16]. Following Eq.

(3) we have

$$\left|\frac{\partial \mathbf{t}}{\partial z}\right| = |\boldsymbol{\beta} \times \mathbf{t}| = |\boldsymbol{\beta}| \sin\theta = \gamma \sin\theta, \tag{7}$$

where we used $|\mathbf{t}| = 1$. θ is the angle between the rotation vector $\boldsymbol{\beta}$ and the polarization state $\mathbf{t}$ and is needed to deduce local retardation. With only a single input state this angle is generally unknown. Conventionally, at least two input polarization states are employed to solve Eq. (3) vectorially and recover the orientation of the apparent optic axis and the amount of scalar local retardation. Owing to the discovered properties of the mirror state, the evolution of $\mathbf{t}$ is constrained to go through $\mathbf{m}$, and it becomes possible to recover both the orientation and the norm of $\boldsymbol{\beta}$ from measurements with only a single input polarization state. Both $\partial\mathbf{t}/\partial z$ and $(\mathbf{m} - \mathbf{t})$ lie within the same plane orthogonal to $\boldsymbol{\beta}$. Hence, the direction of $\boldsymbol{\beta}$ can be obtained by the cross-product $\boldsymbol{\beta}_0 = (\partial\mathbf{t}/\partial z) \times (\mathbf{m} - \mathbf{t})$, and $\sin\theta = \left|\boldsymbol{\beta}_0 \times \mathbf{t}\right| / \left|\boldsymbol{\beta}_0\right|$, allowing to calculate, after some algebraic manipulations:

$$\boldsymbol{\beta} = \frac{\dfrac{\partial \mathbf{t}}{\partial z} \times (\mathbf{m} - \mathbf{t})}{\mathbf{t}^{\top} \cdot (\mathbf{t} - \mathbf{m})}. \tag{8}$$

The norm of $\boldsymbol{\beta}$, scaled to degrees of retardation per depth (°/μm), reveals the sample's local retardation γ. A remaining challenge manifests whenever $\mathbf{t}$ aligns with $\boldsymbol{\beta}$. This corresponds to a vanishing angle θ. In this case the polarization state at a given depth aligns with the fast or slow optic axis of the medium and it ceases to evolve. Using circularly polarized input light requires a half wave of retardation to realize this alignment, which is uncommon in many biological samples. Yet, some tissues feature substantial birefringence and controlling the input state is not necessarily possible. Furthermore, alignment of $\mathbf{t}$ with $\mathbf{m}$ introduces numerical instability, as both the nominator and the denominator in Eq. (8) vanish, making the result more susceptible to noise.

To mitigate the reconstruction artifacts resulting from alignment between $\mathbf{t}$ and $\boldsymbol{\beta}$ or $\mathbf{m}$, we capitalize on the presence of polarization mode dispersion (PMD) in the imaging system and use spectral binning for reconstruction by dividing the spectrum into several overlapping bins [29]. While fiber-based systems may feature strong PMD (artifacts), residual amounts of PMD are present even in free-space PS-OCT systems. Because PMD disperses the input polarization state across the spectral bins, simultaneous alignment of $\mathbf{t}$ with $\boldsymbol{\beta}$ or $\mathbf{m}$ in all bins is very unlikely. We can thus obtain an estimation of the apparent rotation vector $\boldsymbol{\beta}$ individually for each spectral bin. After compensating for PMD by aligning the rotation vectors between the bins we can then compute a weighted mean across the bins, taking into account the reliability of each estimation according to the angle between the apparent rotation vector and the polarization state.

For spectral binning, we multiplied the background-subtracted spectral fringe data interpolated to linear-in-wavenumber k with Hanning windows $h(k,\ n)$ of width $\Delta k/N$ centered on $n\Delta k/(2N)$ within the available k-support Δk, $n \in [1, 2N-1]$, $N = 5$, resulting in 9 spectral bins. For each bin n, we computed the four-component Stokes vectors $[I, Q, U, V]^{\top}$, averaged in the lateral direction with a Gaussian window of full width at half maximum f_w before computing the degree of polarization $\mathrm{DOP} = \left\langle \left(Q^2 + U^2 + V^2\right)^{1/2} / I \right\rangle$, where $\langle\rangle$ indicates averaging over the spectral bins. Finally, the normalized three-components Stokes vector $\mathbf{r}(p,\ l,\ n)$ is recovered for each bin n at each axial position p and lateral location l. To reconstruct $\boldsymbol{\beta}(p,\ l,\ n)$ according to Eq. (8), we approximated $\mathbf{t} \approx (\mathbf{r}\,(p+1) + \mathbf{r}\,(p))/2$ and $\partial\mathbf{t}/\partial z \approx (\mathbf{r}\,(p+1) - \mathbf{r}\,(p))/\Delta z$, where Δz is the axial sampling distance. To express the reliability w of each estimated rotation vector, we use $\sin(\theta)$ by computing $w(p,\ l,\ n) = |\partial\mathbf{t}/\partial z| / |\boldsymbol{\beta}|$. The rotation vectors $\boldsymbol{\beta}(p,\ l,\ n)$ of the various spectral bins all describe the same sample birefringence but are offset in their relative orientation due to system PMD. The required rotation $\mathbf{R}(n)$ to align the rotation vectors of each bin to the central bin N in the least-square sense is given by:

$$\max_{\mathbf{R}(n)} \mathrm{Tr}\left(\mathbf{R}(n)\cdot\sum_{p,\,l}\boldsymbol{\beta}(p,\ l,\ N)\cdot\boldsymbol{\beta}^{\top}(p,\ l,\ N)w(p,\ l,\ n)w(p,\ l,\ N)\right). \tag{9}$$

$\mathbf{R}(n)$ is assumed constant within an entire B-scan, and the sum is taken over all points with sufficient DOP > 0.8 and signal to noise ratio SNR > 8 dB. From the singular value decomposition of the 3×3 matrix defined by the summation $\sum\boldsymbol{\beta}\cdot\boldsymbol{\beta}^{\top}ww = \mathbf{U}\cdot\mathbf{W}\cdot\mathbf{V}^{\dagger}$, the solution to Eq. (9) is obtained by $\mathbf{R} = \mathbf{V}\cdot\mathbf{U}^{\dagger}$. Lastly, the aligned rotation vectors $\mathbf{R}(n)\cdot\boldsymbol{\beta}(p,\ l,\ n)$ are averaged among the spectral bins considering their weights $w(p,\ l,\ n)$. Before taking the vector norm to obtain the final local retardation image, an additional axial averaging over a range h_z is performed. The effect of this last averaging is similar to directly computing the finite difference $\partial\mathbf{t}/\partial z$ over an axial range of h_z pixels.

4.2. Sample imaging

To validate the ability of the polarization mirror state to enable reconstruction of local retardation with a single input polarization state we imaged a tissue-like phantom consisting of a first layer with a long birefringent band and a second layer with four parallel segments with distinct birefringence levels, oriented at an angle to the band in the first layer. The phantom was imaged twice and flipped around in between measurements to have either of the two layers facing up (Fig. 4(a) and Fig. 4(b)).

For comparison, we first evaluated the cumulative retardation by measuring the angle between the Stokes vector $\mathbf{r}$ at each depth and the Stokes vector at the sample surface $\mathbf{r}_{\mathrm{surf}}$. As shown in Figs. 4(c) and 4(d), the cumulative retardation gradually increases within the birefringent areas present in the top layer. The variation in the second layer, however, is less pronounced and depends on the birefringence present in the top layer, which complicates the interpretation of the retardation signal.

To compute local retardation, we calibrated the mirror state $\mathbf{m}$ for each spectral bin by placing an attenuated mirror at the sample location, measuring the returning input polarization state, and mirroring it by the QU-plane, and then reconstructed the local retardation from the phantom data as described above, using $f_w = 13$ A-lines (80 µm) and $h_z = 64$ depth pixels (20 µm). Figures 4(e) and 4(f) present the resulting birefringence maps, which clearly reveal the individual sample segments with their distinct levels of birefringence. The cumulative retardation fundamentally changes when flipping the sample, which precludes a straightforward interpretation of the sample structure. In comparison, the local retardation maps are only minimally impacted by the sample orientation. Moreover, Fig. 4(e, f) compares the processing with and without spectral binning in the rightmost area of the phantom. To ensure fair comparison, the Stokes vectors for both reconstructions are filtered with the same kernel size. Alignment of the backscattered polarization state $\mathbf{t}$ with the mirror state $\mathbf{m}$ in the second layer of the sample leads to an artificial overestimation of the sample birefringence, which is largely suppressed when using spectral binning.

Next, to demonstrate local retardation imaging in biological tissue, we imaged swine retina *ex vivo*. The scanning area centered on the optical nerve head, spanning an area of 6 mm by 6 mm, recording 1024 A-scans along each lateral dimension. Figures 4(g-j) show cross-sectional and *en face* views of local retardation in the excised retina, processed with a three-dimensional Gaussian kernel that spans $h_z = 20\mu$m in the axial direction and $f_w = 60\mu$m in both lateral directions. The cross-sectional intensity image displayed in Fig. 4(g) visualizes the layered structure of the retina. The local retardation reveals the distinct microstructure of the axons in the retinal nerve fiber layer (RNFL), clearly differentiating it from the less birefringent subsequent layers Fig. 4(h). After manually segmenting the upper and lower boundary of the RNFL in each frame, we averaged the intensity and retardation values within the RNFL along depth to generate the *en face* projections

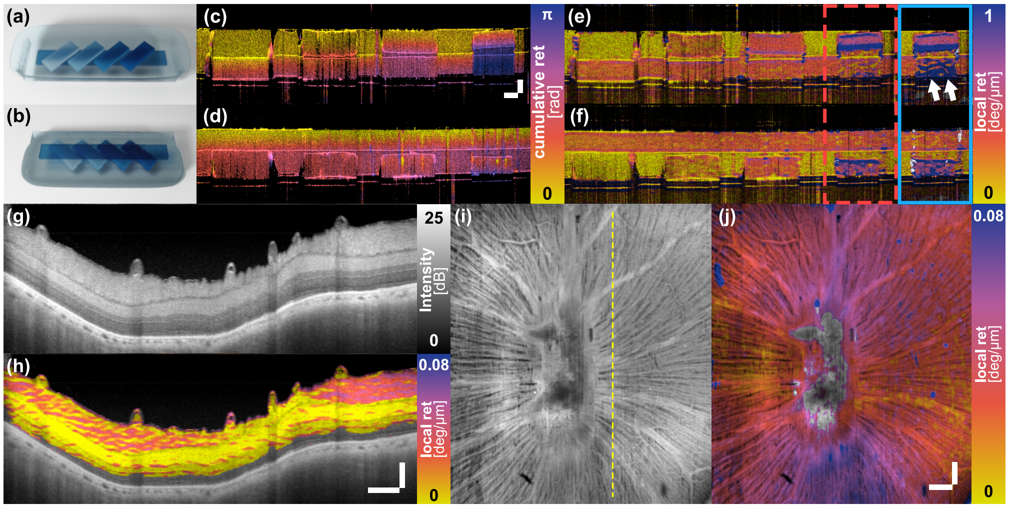

Fig. 4. Local retardation imaging of birefringence phantom and swine retina *ex vivo* using the polarization mirror state constraint. (a, b) Schematic sketch of the two-layer phantom sample in either orientation. (c, d) Corresponding cumulative retardation and (e, f) local retardation images, respectively. The blue box displays the local retardation image of the sample area within the red dashed box reconstructed without spectral binning. The alignment of the polarization state with the mirror state caused by the first birefringent element leads to an overestimation of the birefringence in the second layer (white arrows). Scale bars in (c) measure 100 μm (vertical) and 400 μm (horizontal). (g) Cross-sectional intensity image of swine retina. (h) Cross-sectional local retardation image. Scale bars in (h) measure 100 μm (vertical) and 400 μm (horizontal) and apply to (g, h). (i) Intensity and (j) local retardation *en face* projections of the RNFL layer of the swine retina. The dashed line in (i) indicates the location of the cross-section in (g, h). Both scale bars in (j) measure 400 μm and apply to (i, j). Sample areas in (h) and (j) with a DOP<0.8 are masked.

presented in Figs. 4(i) and 4(j). The *en face* local retardation map exhibits a specific hourglass pattern, featuring higher birefringence in the vertical than along the horizontal direction. This is quite different from the C-shaped RNFL birefringence maps reported in humans [30] but requires further investigation before drawing any conclusions. RNFL birefringence is being investigated for its potential in diagnosing early degeneration of the RNFL associated with glaucoma [31,32].

The phantom and retinal imaging presented in Fig. 4 has been performed with a free-space PS-OCT system and carefully adjusted input polarization states. Yet, the mirror state continues to manifest in fiber and catheter-based imaging systems, where additional optical components break the apparent D-transpose symmetry, and the light propagates through a spinning optical fiber which dynamically alters the polarization state incident on the sample. To evidence the ability to reconstruct local retardation with a single input state in a catheter-based system, we processed data from a cylindrical birefringence phantom (Fig. 5(a)) acquired previously with an intravascular PS-OFDI system [23]. The system modulated the input polarization state between even and odd A-lines, and conventional reconstruction of local retardation with spectral binning [29] as shown in Fig. 5(b) was used for comparison. $f_w = 12$ A-lines was used for lateral filtering of the Stokes vectors across the rotational scans consisting of 2048 A-lines, with $h_z = 5$ depth pixels (30 μm). We then reconstructed local retardation using only the 1024 even A-lines of the data, reducing the filter to $f_w = 6$ to maintain identical angular averaging. Collecting the A-line centered in the middle of the birefringent band out of each frame we created the cross-sectional image along the longitudinal direction. Because calibration of the mirror state was not possible in this case, to identify the mirror state we generated 2D histograms of the polarization states as a function of their azimuth and elevation angle on the Poincaré sphere, evaluated only in areas with DOP > 0.8 and SNR > 10 dB for each spectral bin in an entire B-scan. Akin to the fiber twisting experiment, the round-trip retardation through the spinning catheter and the birefringent sample ensured repeated evolution through the mirror state. The computed histograms indeed featured a well-defined mode that we selected as the mirror state for each bin, and enabled reconstruction of local retardation as displayed in Fig. 5(c). The mirror states were stable across entire pullbacks. The longitudinal cross-sections of both the two input states and the single input state reconstruction present very comparable birefringence maps.

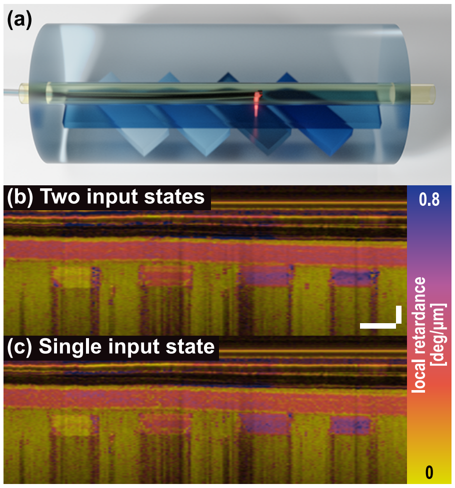

Fig. 5. Birefringence phantom imaging using a catheter-based PS-OFDI. (a) Schematic sketch of the cylindrical birefringence phantom. (b, c) Cross-sectional birefringence images along the pullback direction, reconstructed using conventional two input polarization states processing (b) and from only a single input state, using the mirror state constraint for reconstruction (c). Scale bars in (b) measure 250 μm (vertical) and 1 mm (horizontal) and apply to (b, c).

5. Discussion

This study reports how the evolution of the polarization state after round-trip propagation through a medium with changing retardation is constrained to pass through the polarization mirror state. In addition to experimental demonstration and theoretical derivation of this constraint, we show how it enables the reconstruction of local retardation, both in free-space and fiber-based PS-OCT systems, from measurements with a single, unknown input polarization state. Leveraging from modest spectral variations in the polarization state transmitted through static system components, we further prevent obscuration of sample birefringence because alignment of the polarization state with the sample optic axis across the entire spectrum is improbable.

Single input state PS-OCT has traditionally been limited to measuring cumulative retardation. In samples composed of several retarding layers with distinct optic axis orientations, the cumulative retardation produces a very convolved picture of the sample birefringence that is difficult to interpret. While the benefit of local retardation imaging has been well established [33,34], integrating hardware for modulating or multiplexing two input states in addition to the required polarization diverse detection further increases system complexity. Any simplification of the system architecture may enable a more widespread adoption of local retardation imaging with PS-OCT. Fan and Yao previously introduced a reconstruction strategy to recover local retardation from measurements with only a single input polarization state [35,36]. Their approach relies on the round-trip symmetry of the imaging system and the circularity of the input polarization state and is incompatible with fiber and catheter-based systems. The mirror state and the resulting constraint on the evolution of the depth-dependent polarization state described in this manuscript extends the ability to reconstruct local retardation from measurements with a single input polarization state to these important practical settings.

The mirror state corresponds to the polarization state of light reflected at the sample location and mirrored by a symmetry plane in the Poincaré sphere. The rotation of the QU-plane by the single-pass transmission from the reflector's location to the detector defines the plane of symmetry. Directly calibrating the mirror state is thus challenging, as it requires detailed characterization of the system transmission, achieved in our initial experiments by using a free-space system with known identity transmissions. Conveniently, in fiber-based systems, the mirror state can be obtained by estimating the most frequently realized polarization state returned from a sample with diverse birefringence. Twisting the fiber to dynamically modulate the transmission through the fiber can be used to enrich the birefringence realizations. In case of a catheter-based system, this is intrinsically achieved by rotating the catheter. Interestingly, this calibration strategy directly provides the mirror state, without knowledge of the symmetry plane or the 'input' polarization state. Our experimental results with catheter-based measurements clearly demonstrate the robustness and effectiveness of our approach in this practical setting and offer a pathway to simplified system architectures for catheter-based PS imaging.

Combination of the mirror state constraint with spectral binning proved crucial to obtain robust and reliable local retardation measurements. Without binning, alignment of polarization state with the optic axis of the sample can occasionally happen, as captured by the reliability metric. Strikingly, even the residual amounts of spectral variation in the input polarization state prepared with achromatic wave plates in case of our free space experiments markedly improved the recovered birefringence maps. In case of fiber-based systems, the circulators are likely the dominant source of more substantial PMD. Of note, we align the rotation vectors between the spectral bins with a rotation that is constant across the entire B-scan, which assumes that the PMD is induced in the static part of the system and that wavelength-dependent birefringence in the sample or PMD in the rotating catheter can be neglected. Also, the presence of diattenuation that induces polarization-dependent loss cannot be captured with the presented SO(3) formalism. Diattenuation, or dichroism, is considered to be small compared to retardation in typical samples and tissues [37–39], but would skew the measured polarization states and frustrate the manifestation of the mirror state.

6. Conclusion

In conclusion, we demonstrated the peculiar properties of the mirror polarization state that manifest when measuring backscattered light along identical illumination and detection paths free of polarization-dependent loss. In PS-OCT the mirror state constrains the evolution of the depth-dependent polarization state and enables local retardation imaging using only a single input polarization state. Combined with spectral binning, which mitigates the detrimental impact of the polarization state aligning with the sample's optic axis, we obtained convincing local retardation images both in free-space and through a fiber-based spinning catheter. The redundancy of a second input polarization state offers a critical simplification of the hardware required for performing local retardation imaging and may facilitate clinical and commercial adoption of PS-OCT imaging.

A. Appendix

A.1. Mueller matrix of reverse transmission through a reciprocal medium

In this section, we derive the deterministic (i.e. non-depolarizing) Mueller matrix of the reverse transmission through a reciprocal element from its corresponding Jones expression. If A and B denote the front and rear interface of this element, the Jones matrix $\mathbf{J}_{\mathrm{AB}}$ describes the forward propagation through this element (as shown in Fig. 6). The reverse transmission is given by the transpose of this matrix $\mathbf{J}_{\mathrm{BA}} = \mathbf{J}_{\mathrm{AB}}^{\top}$, when maintaining the orientation of the spatial xy-coordinates irrespective of the propagation direction [24].

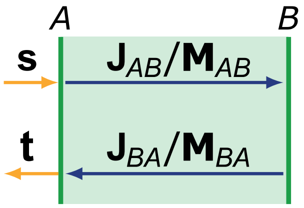

Fig. 6. Schematic diagram of the transmission through an element from A to B and in the reverse direction, described by the Jones and Mueller matrices, respectively.

A matrix $\mathbf{J}$ in the Jones formalism can be converted into its corresponding Mueller matrix $\mathbf{M}$ using [40].

$$\mathbf{M} = \mathbf{U} \cdot (\mathbf{J} \otimes \mathbf{J}^{*}) \cdot \mathbf{U}^{\dagger}$$

$$\mathbf{U} = \frac{1}{\sqrt{2}} \begin{bmatrix} 1 & 0 & 0 & 1 \\ 1 & 0 & 0 & -1 \\ 0 & 1 & 1 & 0 \\ 0 & i & -i & 0 \end{bmatrix}, \tag{10}$$

where $\otimes$ is the Kronecker tensor product, $\mathbf{J}^{*}$ is the complex conjugate of $\mathbf{J}$, and $\mathbf{U}^{\dagger}$ represents the conjugate transpose of $\mathbf{U}$, corresponding also to its inverse. Using the fact that the transpose is distributive for the Kronecker product ($(\mathbf{A} \otimes \mathbf{B})^{\top} = \mathbf{A}^{\top} \otimes \mathbf{B}^{\top}$), we find

$$\begin{aligned} \mathbf{M}_{\mathrm{BA}} &= \mathbf{U} \cdot \left(\mathbf{J}_{\mathrm{BA}} \otimes \mathbf{J}_{\mathrm{BA}}^{*}\right) \cdot \mathbf{U}^{\dagger} \\ &= \mathbf{U} \cdot \left(\mathbf{J}_{\mathrm{AB}}^{\top} \otimes \mathbf{J}_{\mathrm{AB}}^{\dagger}\right) \cdot \mathbf{U}^{\dagger} \\ &= \mathbf{U} \cdot \left(\mathbf{J}_{\mathrm{AB}} \otimes \mathbf{J}_{\mathrm{AB}}^{*}\right)^{\top} \cdot \mathbf{U}^{\dagger} \\ &= \mathbf{U} \cdot \mathbf{I} \cdot \left(\mathbf{J}_{\mathrm{AB}} \otimes \mathbf{J}_{\mathrm{AB}}^{*}\right)^{\top} \cdot \mathbf{I} \cdot \mathbf{U}^{\dagger} \\ &= \mathbf{U} \cdot \left(\mathbf{U}^{\top} \cdot \mathbf{U}^{*}\right) \cdot \left(\mathbf{J}_{\mathrm{AB}} \otimes \mathbf{J}_{\mathrm{AB}}^{*}\right)^{\top} \cdot \left(\mathbf{U}^{\top} \cdot \mathbf{U}^{*}\right) \cdot \mathbf{U}^{\dagger} \\ &= \left(\mathbf{U} \cdot \mathbf{U}^{\top}\right) \cdot \mathbf{U}^{*} \cdot \left(\mathbf{J}_{\mathrm{AB}} \otimes \mathbf{J}_{\mathrm{AB}}^{*}\right)^{\top} \cdot \mathbf{U}^{\top} \cdot \left(\mathbf{U}^{*} \cdot \mathbf{U}^{\dagger}\right) \\ &= \left(\mathbf{U} \cdot \mathbf{U}^{\top}\right) \cdot \mathbf{M}_{\mathrm{AB}}^{\top} \cdot \left(\mathbf{U}^{*} \cdot \mathbf{U}^{\dagger}\right). \end{aligned} \tag{11}$$

Evaluating the outermost expressions, we find $\mathbf{U} \cdot \mathbf{U}^{\top} = \mathbf{U}^{*} \cdot \mathbf{U}^{\dagger} = \mathrm{diag}(1, 1, 1, -1)$. The transpose of a Jones matrix corresponds to the transpose of its corresponding Mueller matrix, with the sign of the last row and column, excluding the on-diagonal element, inverted. It represents the reverse transmission through a reciprocal element. For a pure retardation matrix $\mathbf{R}$ in the SO(3) formalism, this results in $\mathbf{R}_{\mathrm{BA}} = \mathbf{D} \cdot \mathbf{R}_{\mathrm{AB}}^{\top} \cdot \mathbf{D}$, where $\mathbf{D} = \mathrm{diag}(1, 1, -1)$.

A.2. Determination of rotation vector

The effect of a linear retarder can be expressed as a rotation vector $\boldsymbol{\tau} = \varphi \cdot \boldsymbol{\tau}_0 = \varphi \cdot [\cos\alpha, \sin\alpha, 0]^\top$, where $\boldsymbol{\tau}_0$ has unitary length, α is the azimuth angle with respect to the Q-axis and φ is the rotation angle, i.e. the amount of retardation. Assuming the linear retarder describes a homogeneous layer of thickness Δz, its rotation axis $\boldsymbol{\tau}$ is identical to that of the differential matrix, and its retardation is $\varphi = \gamma\Delta z$. The corresponding SO(3) rotation matrix $\mathbf{T}$ is [41]:

$$\begin{aligned}\mathbf{T} &= \mathbf{I} + \sin\varphi \cdot \mathbf{K} + (1-\cos\varphi)\,\mathbf{K}^2 = \exp(\varphi\mathbf{K})\\ \mathbf{K} &= \begin{bmatrix} 0 & \tau_3 & -\tau_2 \\ -\tau_3 & 0 & \tau_1 \\ \tau_2 & -\tau_1 & 0 \end{bmatrix} = \begin{bmatrix} 0 & 0 & -\sin\alpha \\ 0 & 0 & \cos\alpha \\ \sin\alpha & -\cos\alpha & 0 \end{bmatrix}.\end{aligned} \tag{12}$$

Here, we are looking for the linear retarder $\mathbf{T}(\varphi, \alpha)$ that maps an input state $\mathbf{s} = [s_1, s_2, s_3]^\top$ to some state $\mathbf{t} = [t_1, t_2, t_3]^\top$. Its rotation axis is given by the intersection of the QU-plane and the plane bisecting $\mathbf{s}$ and $\mathbf{t}$:

$$(\mathbf{t}-\mathbf{s}) \times \begin{bmatrix} 0 \\ 0 \\ 1 \end{bmatrix} = \begin{bmatrix} t_2 - s_2 \\ s_1 - t_1 \\ 0 \end{bmatrix}, \tag{13}$$

from where

$$\alpha = \tan^{-1}\left(\frac{s_1 - t_1}{t_2 - s_2}\right). \tag{14}$$

In general, $\mathbf{s}$ and $\mathbf{t}$ clearly define a single rotation axis. Only for the mirror polarization state, in which case both the nominator and denominator vanish, α is undefined and can take any value. To find the amount of rotation around this axis required to map $\mathbf{s}$ onto $\mathbf{t}$, we project both vectors onto the plane orthogonal to the rotation axis and evaluate their relative angle:

$$\begin{aligned}\varphi &= \cos^{-1}\left(\frac{\left(\mathbf{s} - (\boldsymbol{\tau}_0^\top \cdot \mathbf{s}) \cdot \boldsymbol{\tau}_0\right)^\top \cdot \left(\mathbf{t} - (\boldsymbol{\tau}_0^\top \cdot \mathbf{t}) \cdot \boldsymbol{\tau}_0\right)}{\sqrt{1 - \left(\boldsymbol{\tau}_0^\top \cdot \mathbf{s}\right)^2}\sqrt{1 - \left(\boldsymbol{\tau}_0^\top \cdot \mathbf{t}\right)^2}}\right)\\ &= \cos^{-1}\left(\frac{\mathbf{s}^\top \cdot \mathbf{t} - (\boldsymbol{\tau}_0^\top \cdot \mathbf{s})^2}{1 - \left(\boldsymbol{\tau}_0^\top \cdot \mathbf{s}\right)^2}\right),\end{aligned} \tag{15}$$

where $\boldsymbol{\tau}_0 = [\cos\alpha, \sin\alpha, 0]^\top$, and $\boldsymbol{\tau}_0^\top \cdot \mathbf{s} = \boldsymbol{\tau}_0^\top \cdot \mathbf{t}$ by construction. A defined rotation vector $\boldsymbol{\tau}$ within the QU-plane maps $\mathbf{s}$ onto a general $\mathbf{t}$. Only for the mirror state $\mathbf{t} = \mathbf{m}$, there exists a rotation for any azimuth direction within the QU-plane, tracing out a continuous curve in the QU-plane when wrapped to $\varphi \in (-\pi, \pi)$ (the red curve in Fig. 7(b)).

The shape and orientation of this trace is determined by $\mathbf{s}$. Assuming the azimuth and elevation angles of $\mathbf{s}$ are $\alpha_\mathbf{s}$ and $\varepsilon_\mathbf{s}$, respectively ($\alpha_\mathbf{s} \in [0, 2\pi)$, $\varepsilon_\mathbf{s} \in [-\pi/2, \pi/2]$), then the largest rotation angle $\varphi_\mathrm{A} = \pi$ appears when the rotation vector aligns with the projection of $\mathbf{s}$ onto the QU-plane, indicated by $\boldsymbol{\tau}_{\mathrm{A}0}$ in Fig. 7(a). The smallest rotation angle appears when the rotation axis $\boldsymbol{\tau}_{\mathrm{B}0}$ is perpendicular to $\boldsymbol{\tau}_{\mathrm{A}0}$. In this case the rotation trajectory coincides with a longitude of the sphere and corresponds to a rotation angle of $\varphi_\mathrm{B} = 2\,|\varepsilon_\mathbf{s}|$. As visualized in Fig. 7(b), the long axis of the trace aligns with the azimuth angle of input state $\mathbf{s}$, and the curvature of the trace is determined by the elevation angle of $\mathbf{s}$.

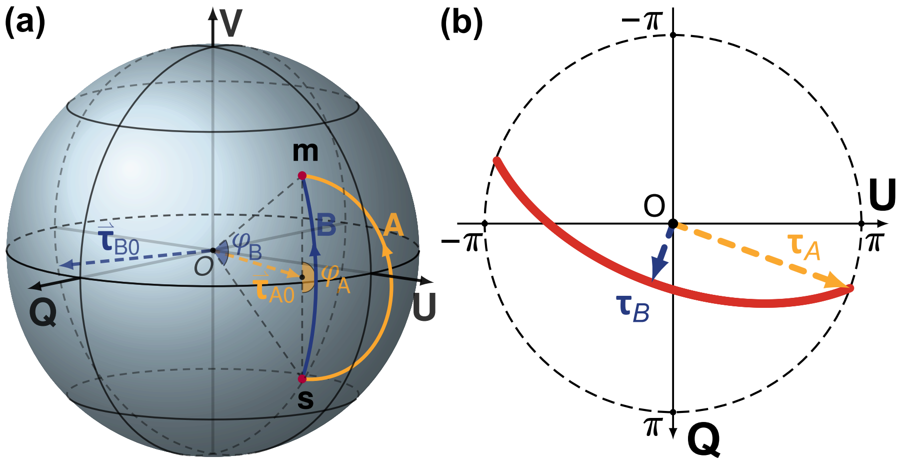

Fig. 7. The trace of the possible rotation vectors that map the input state **s** to its mirror state **m** is defined by the input state. (a) The maximum and minimum rotation angle φ_{A}, φ_{B} and the corresponding rotation axes $\boldsymbol{\tau}_{\mathrm{A}0}$, $\boldsymbol{\tau}_{\mathrm{B}0}$ shown on the Poincare sphere. (b) The corresponding rotation vectors $\boldsymbol{\tau}_{\mathrm{A}}$ and $\boldsymbol{\tau}_{\mathrm{B}}$ define the orientation and curvature of the trace of the possible rotation vectors (red line).

In conclusion, there is always a suitable rotation angle for any orientation of the rotation axis of **T** to achieve $\mathbf{T} \cdot \mathbf{s} = \mathbf{m}$. Left-multiplying this with **D** provides $\mathbf{D} \cdot \mathbf{T} \cdot \mathbf{s} = \mathbf{s}$ which indicates that **s** is invariant to transformation by $\mathbf{D} \cdot \mathbf{T}$ and that **s** is an eigenvector of $\mathbf{D} \cdot \mathbf{T}$ with a unitary eigenvalue.

Funding

National Research Foundation Singapore (NRF-CRP13-2014-05); Ministry of Education - Singapore (2018-T1-001-144); Agency for Science, Technology and Research (H17/01/a0/008); National Institutes of Health (P41EB-015903, R03EB-024803); Terumo Corporation.

Disclosures

QX, NW, XL, BB, LL, MV: Terumo Corporation (P).

References

1. K. Sassen, "The polarization lidar technique for cloud research: A review and current assessment," Bull. Am. Meteorol. Soc. **72**(12), 1848–1866 (1991).
2. J. S. Tyo, D. L. Goldstein, D. B. Chenault, and J. A. Shaw, "Review of passive imaging polarimetry for remote sensing applications," Appl. Opt. **45**(22), 5453–5469 (2006).
3. N. Ghosh and A. I. Vitkin, "Tissue polarimetry: concepts, challenges, applications, and outlook," J. Biomed. Opt. **16**(11), 110801 (2011).
4. V. V. Tuchin, "Polarized light interaction with tissues," J. Biomed. Opt. **21**(7), 071114 (2016).
5. J. Qi and D. S. Elson, "Mueller polarimetric imaging for surgical and diagnostic applications: a review," J. Biophotonics **10**(8), 950–982 (2017).
6. M. R. Hee, D. Huang, E. A. Swanson, and J. G. Fujimoto, "Polarization-sensitive low-coherence reflectometer for birefringence characterization and ranging," J. Opt. Soc. Am. B **9**(6), 903–908 (1992).
7. J. F. De Boer, C. K. Hitzenberger, and Y. Yasuno, "Polarization sensitive optical coherence tomography–a review," Biomed. Opt. Express **8**(3), 1838–1873 (2017).
8. B. Baumann, "Polarization sensitive optical coherence tomography: a review of technology and applications," Appl. Sci. **7**(5), 474 (2017).
9. J. F. De Boer, T. E. Milner, M. J. van Gemert, and J. S. Nelson, "Two-dimensional birefringence imaging in biological tissue by polarization-sensitive optical coherence tomography," Opt. Lett. **22**(12), 934–936 (1997).

10. C. K. Hitzenberger, E. Götzinger, M. Sticker, M. Pircher, and A. F. Fercher, "Measurement and imaging of birefringence and optic axis orientation by phase resolved polarization sensitive optical coherence tomography," Opt. Express **9**(13), 780–790 (2001).
11. C. E. Saxer, J. F. de Boer, B. H. Park, Y. Zhao, Z. Chen, and J. S. Nelson, "High-speed fiber–based polarization-sensitive optical coherence tomography of in vivo human skin," Opt. Lett. **25**(18), 1355–1357 (2000).
12. S. Guo, J. Zhang, L. Wang, J. S. Nelson, and Z. Chen, "Depth-resolved birefringence and differential optical axis orientation measurements with fiber-based polarization-sensitive optical coherence tomography," Opt. Lett. **29**(17), 2025–2027 (2004).
13. M. Todorović, S. Jiao, L. V. Wang, and G. Stoica, "Determination of local polarization properties of biological samples in the presence of diattenuation by use of Mueller optical coherence tomography," Opt. Lett. **29**(20), 2402–2404 (2004).
14. S. Makita, M. Yamanari, and Y. Yasuno, "Generalized Jones matrix optical coherence tomography: performance and local birefringence imaging," Opt. Express **18**(2), 854–876 (2010).
15. C. Fan and G. Yao, "Full-range spectral domain Jones matrix optical coherence tomography using a single spectral camera," Opt. Express **20**(20), 22360–22371 (2012).
16. M. Villiger, D. Lorenser, R. A. McLaughlin, B. C. Quirk, R. W. Kirk, B. E. Bouma, and D. D. Sampson, "Deep tissue volume imaging of birefringence through fibre-optic needle probes for the delineation of breast tumour," Sci. Rep. **6**(1), 28771 (2016).
17. N. Wang, X. Liu, Q. Xiong, J. Xie, S. Chen, and L. Liu, "Polarization management to mitigate misalignment-induced fringe fading in fiber-based optical coherence tomography," Opt. Lett. **42**(15), 2996–2999 (2017).
18. E. Brinkmeyer, "Forward-backward transmission in birefringent single-mode fibers: interpretation of polarization-sensitive measurements," Opt. Lett. **6**(11), 575–577 (1981).
19. M. O. Van Deventer, "Polarization properties of Rayleigh backscattering in single-mode fibers," J. Lightwave Technol. **11**(12), 1895–1899 (1993).
20. F. Corsi, "Polarization mode dispersion characterization of single-mode optical fiber using backscattering technique," J. Lightwave Technol. **16**(10), 1832–1843 (1998).
21. Q. Xiong, N. Wang, X. Liu, S. Chen, H. Liang, S. Chen, and L. Liu, "Single input state polarization-sensitive optical coherence tomography with high resolution and polarization distortion correction," Opt. Express **27**(5), 6910–6924 (2019).
22. M. Mujat, B. H. Park, B. Cense, T. C. Chen, and J. F. de Boer, "Autocalibration of spectral-domain optical coherence tomography spectrometers for in vivo quantitative retinal nerve fiber layer birefringence determination," J. Biomed. Opt. **12**(4), 041205 (2007).
23. X. Liu, K. Beaudette, X. Wang, L. Liu, B. E. Bouma, and M. Villiger, "Tissue-like phantoms for quantitative birefringence imaging," Biomed. Opt. Express **8**(10), 4454–4465 (2017).
24. N. Vansteenkiste, P. Vignolo, and A. Aspect, "Optical reversibility theorems for polarization: application to remote control of polarization," J. Opt. Soc. Am. A **10**(10), 2240–2245 (1993).
25. S. R. Cloude and E. Pottier, "Concept of polarization entropy in optical scattering," Opt. Eng. **34**(6), 1599–1611 (1995).
26. R. J. Potton, "Reciprocity in optics," Rep. Prog. Phys. **67**(5), 717–754 (2004).
27. J. J. Gil, "Polarimetric characterization of light and media: physical quantities involved in polarimetric phenomena," Eur. Phys. J.: Appl. Phys. **40**(1), 1–47 (2007).
28. M. Villiger, B. Braaf, N. Lippok, K. Otsuka, S. K. Nadkarni, and B. E. Bouma, "Optic axis mapping with catheter-based polarization-sensitive optical coherence tomography," Optica **5**(10), 1329–1337 (2018).
29. M. Villiger, E. Z. Zhang, S. K. Nadkarni, W.-Y. Oh, B. J. Vakoc, and B. E. Bouma, "Spectral binning for mitigation of polarization mode dispersion artifacts in catheter-based optical frequency domain imaging," Opt. Express **21**(14), 16353–16369 (2013).
30. J. Willemse, M. G. O. Gräfe, J. A. van de Kreeke, F. Feroldi, F. D. Verbraak, and J. F. de Boer, "Optic axis uniformity as a metric to improve the contrast of birefringent structures and analyze the retinal nerve fiber layer in polarization-sensitive optical coherence tomography," Opt. Lett. **44**(15), 3893–3896 (2019).
31. B. Cense, T. C. Chen, B. H. Park, M. C. Pierce, and J. F. de Boer, "In vivo depth-resolved birefringence measurements of the human retinal nerve fiber layer by polarization-sensitive optical coherence tomography," Opt. Lett. **27**(18), 1610–1612 (2002).
32. M. Pircher, C. K. Hitzenberger, and U. Schmidt-Erfurth, "Polarization sensitive optical coherence tomography in the human eye," Prog. Retinal Eye Res. **30**(6), 431–451 (2011).
33. S. Sugiyama, Y.-J. Hong, D. Kasaragod, S. Makita, S. Uematsu, Y. Ikuno, M. Miura, and Y. Yasuno, "Birefringence imaging of posterior eye by multi-functional Jones matrix optical coherence tomography," Biomed. Opt. Express **6**(12), 4951–4974 (2015).
34. M. Villiger, K. Otsuka, A. Karanasos, P. Doradla, J. Ren, N. Lippok, M. Shishkov, J. Daemen, R. Diletti, R.-J. van Geuns, F. Zijlstra, G. van Soest, P. Libby, E. Regar, S. K. Nadkarni, and B. E. Bouma, "Coronary plaque microstructure and composition modify optical polarization: a new endogenous contrast mechanism for optical frequency domain imaging," JACC: Cardiovascular Imaging **11**(11), 1666–1676 (2018).
35. C. Fan and G. Yao, "Mapping local retardance in birefringent samples using polarization sensitive optical coherence tomography," Opt. Lett. **37**(9), 1415–1417 (2012).

36. C. Fan and G. Yao, "Mapping local optical axis in birefringent samples using polarization-sensitive optical coherence tomography," J. Biomed. Opt. **17**(11), 110501 (2012).
37. B. H. Park, M. C. Pierce, B. Cense, and J. F. de Boer, "Jones matrix analysis for a polarization-sensitive optical coherence tomography system using fiber-optic components," Opt. Lett. **29**(21), 2512–2514 (2004).
38. N. J. Kemp, H. N. Zaatari, J. Park, H. G. Rylander III, and T. E. Milner, "Form-biattenuance in fibrous tissues measured with polarization-sensitive optical coherence tomography (PS-OCT)," Opt. Express **13**(12), 4611–4628 (2005).
39. B. Baumann, S. O. Baumann, T. Konegger, M. Pircher, E. Götzinger, F. Schlanitz, C. Schütze, H. Sattmann, M. Litschauer, U. Schmidt-Erfurth, and C. K. Hitzenberger, "Polarization sensitive optical coherence tomography of melanin provides intrinsic contrast based on depolarization," Biomed. Opt. Express **3**(7), 1670–1683 (2012).
40. C. F. Bohren and D. R. Huffman, *Absorption and Scattering of Light by Small Particles* (John Wiley & Sons, 2008).
41. J. Gordon and H. Kogelnik, "PMD fundamentals: Polarization mode dispersion in optical fibers," Proc. Natl. Acad. Sci. **97**(9), 4541–4550 (2000).